PROCEEDINGS OF SPIE

SPIEDigitalLibrary.org/conference-proceedings-of-spie

A combined ultrasound and photoacoustic imaging platform for clinical research applications

Weylan Thompson, Hans-Peter Brecht, Sergey Ermilov, Vassili Ivanov

Weylan Thompson, Hans-Peter Brecht, Sergey A. Ermilov, Vassili Ivanov, "A combined ultrasound and photoacoustic imaging platform for clinical research applications," Proc. SPIE 11960, Photons Plus Ultrasound: Imaging and Sensing 2022, 119600K (3 March 2022); doi: 10.1117/12.2610099

SPIE.

Event: SPIE BiOS, 2022, San Francisco, California, United States

A combined ultrasound and photoacoustic imaging platform for clinical research applications

Weylan R. Thompson, Dylan J. Lawrence, Hans-Peter Brecht, Sergey A. Ermilov, Vassili Ivanov

PhotoSound Technologies, Inc., 9511 Town Park Dr., Houston, Texas 77036, USA

ABSTRACT

We present the continued development of a clinical ultrasound (US) imaging device with an enabled photoacoustic (PA) mode. The combined USPA imaging platform is designed around a compact US component capable of B-mode, M-mode, color Doppler, and pulsed wave Doppler US imaging with a 128 element US probe. The PA mode can support a 256 element PA probe over two 128-channel connectors with real-time 2D imaging at frame rates up to 20 Hz. PA signals are amplified by a 40 dB pre-amp and have an additional programmable gain of 6-51 dB; US mode signals bypass the pre-amp circuit and have a time gain compensation control up to 40 dB. USPA represents a multifunctional imaging platform that can produce quality anatomical and physiological images using the US modes and co-registered physiological and molecular imaging using the PA mode. The software development kit (SDK) released with the device allows for implementation of custom PA imaging algorithms and visualization. We demonstrate the USPA device's capabilities using a 5-14 MHz linear US probe to image phantoms simulating future clinical applications, such as blood oxygen saturation and vascular development.

Keywords: photoacoustic imaging, ultrasound imaging, multimodal imaging, parallel data acquisition, photosound

1. INTRODUCTION

Ultrasound (US) imaging is an established, non-invasive, clinical imaging modality used for real-time anatomical and functional imaging [1, 2]. Its shortfalls in functional imaging come from US's ineffectiveness in specific detection of endogenous chromophores [3]. Photoacoustic (PA) imaging is an emerging noninvasive imaging modality that excels in the high-resolution detection of endogenous and exogenous chromophores by utilizing multi-wavelength light excitation [4-9]. Through the exploitation of the optical absorption spectrum of unique tissue or contrasts, PA imaging can identify the location and quantify relative concentration of a target using spectral unmixing techniques [10, 11]. Thus, a US imaging device combined with a PA imaging mode would reap the benefits of anatomical and non-specific functional imaging from US and specific functional and molecular imaging from PA [12-14]. A synergistic benefit of a USPA system is that both modalities can use the same transducer to detect sound waves, reducing the necessity of complex imaging system geometries, which is convenient for spatially registering US and PA images [15]. For these reasons, a combined USPA imaging system would allow clinical researchers to use a familiar modality (US) and hardware (US probe) while expanding the range of topics to investigate beyond the anatomical and limited functional imaging of US and discover applications for PA in studies.

Continuing our previous work [16], we describe the continued development of an original equipment manufacturer (OEM) USPA system, the MoleculUS (Figure 1:A), an ultrasound system with enhanced molecular imaging through a PA mode. We then demonstrate the system using a US probe with integrated optical fibers and a nanosecond-pulsed laser to image a spatial resolution phantom, a depth sensitivity phantom, and an *in vivo* human wrist.

2. MOLECULUS IMAGING PLATFORM

The MoleculUS is an OEM clinical US device with an added dedicated PA mode (Figure 1:A), the modes have separate analog-to-digital (ADC) acquisitions systems. The USPA device has three main boards and an optional fourth board: US device (Figure 1:B1); USPA adapter (Figure 1:B2); PA device (Figure 1:B3); optional extra PA preamp (Figure 1:B4).

The US device (Figure 1:B1) is an OEM clinical US device (ArtUS, UAB TELEMED, Vilnius, Lithuania) that has the expected US modes (B-mode, M-mode, color Doppler, power Doppler, etc.) and a full software suite with software development kit (SDK). The US modality is only compatible with TELEMED US probes or US probes that have been

Photons Plus Ultrasound: Imaging and Sensing 2022, edited by Alexander A. Oraevsky, Lihong V. Wang
Proc. of SPIE Vol. 11960, 119600K · © 2022 SPIE · 1605-7422 · doi: 10.1117/12.2610099

encoded with TELEMED firmware. Probes with channels up to 128 elements are supported for US and PA, 192 element probes are supported with US only. The US ADC acquires data with 12-bit resolution and has a frequency range of 1.5-18.0 MHz with up to 40 dB signal gain.

Figure 1: MoleculUS system in housing (A). MoleculUS system without housing (B); USPA adapter board (1), US device (2), PA pre-amp board (3), PA ADC (4).

The USPA adapter board (Figure 1:B2) interfaces the US and PA devices through use of a common probe connector (QLC260, ITT Cannon, Irvine, CA, USA). The probe connector's channels are routed to both the US and PA ADCs (Figure 2). For the US signal path, the adapter board uses a multiplexer to transmit data to the US ADC though a 64-channel connection. The US signal is beamformed and processed in the US device then sent to a PC, via USB3 connection, for reconstruction. The multiplexer switch is closed for a US acquisition event and open for a PA acquisition event.

For the PA signal path, the adapter board has a switch that is open when the US mode is active, to guard against high-voltage transmit signals, and closed when the PA mode is active, to acquire the detected signals from the probe. This protective T/R switch allows a 40 dB (50 Ω load over 0.025-45 MHz at -6 dB bandwidth) PA signal amplifier stage to be integrated on the USPA board safely.

The PA device (Figure 1:B3) is an in-house OEM ADC board (LEGION ADC256, PhotoSound Technologies, Houston, TX, USA) that was developed for acquiring PA data [17]. The PA ADC board has 256 channels across two probe connectors, which are fed into four ADC 32-channel chips each, though only 128 channels are enabled for USPA acquisitions. The ADC chips have a 12-bit acquisition resolution, a sampling frequency of 40 MHz, and an analog-front-end (AFE) capable of high pass filtering (cutoff between 75-150 kHz), low pass filtering (cutoff between 5-25 MHz), and amplification (6-51 dB). The PA ADC has a field-programmable gate array (FPGA) controller for onboard programming and transfers data to a PC via a USB3 connection. The 128 PA only channels can be used with an amplifier (Figure 1:B4) if extra transducer channels are required. The 2D real-time reconstruction is limited to 25 Hz, but the PA ADC board is capable of acquiring data at a repetition rate up to 200 Hz at 4096-points per data frame. The

board has four possible trigger inputs: two electrical inputs with either 50 Ω or HiZ input impedance and two optical photodiodes.

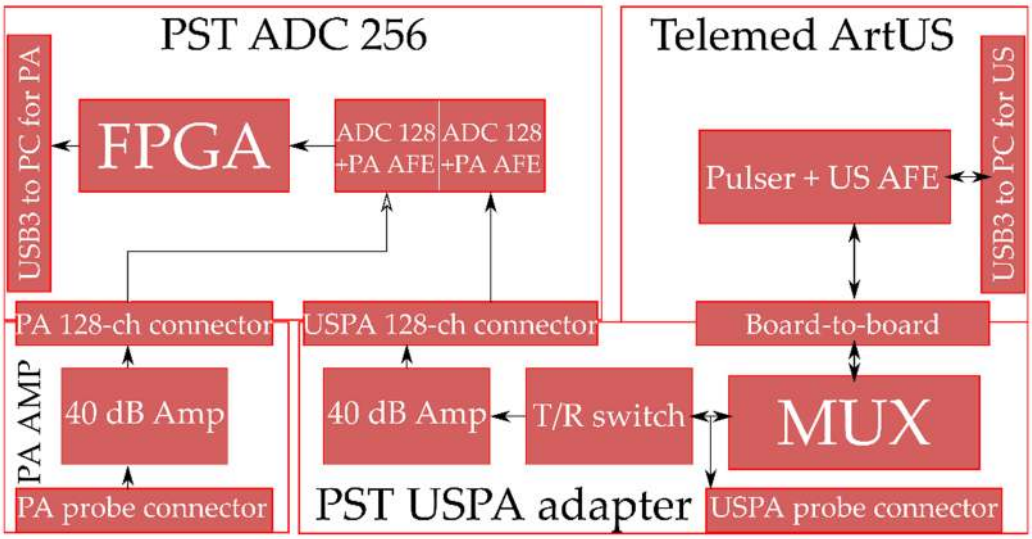

Figure 2: Block-diagram of the USPA device's subsystems.

The USPA communication timing is such that the US mode can be continuously running, independent of the laser excitation of the PA mode, until a PA acquisition event is detected, then the US acquisition event coinciding with the PA event will be dropped (Figure 3). In this scheme, the US mode's operational rate is not sacrificed to match the PA mode's repetition rate. It is also possible to match the US to the PA acquisition events with a specified delay. The delay between the input trigger pulse and PA acquisition is set to 200 µs to suppress transient signals.

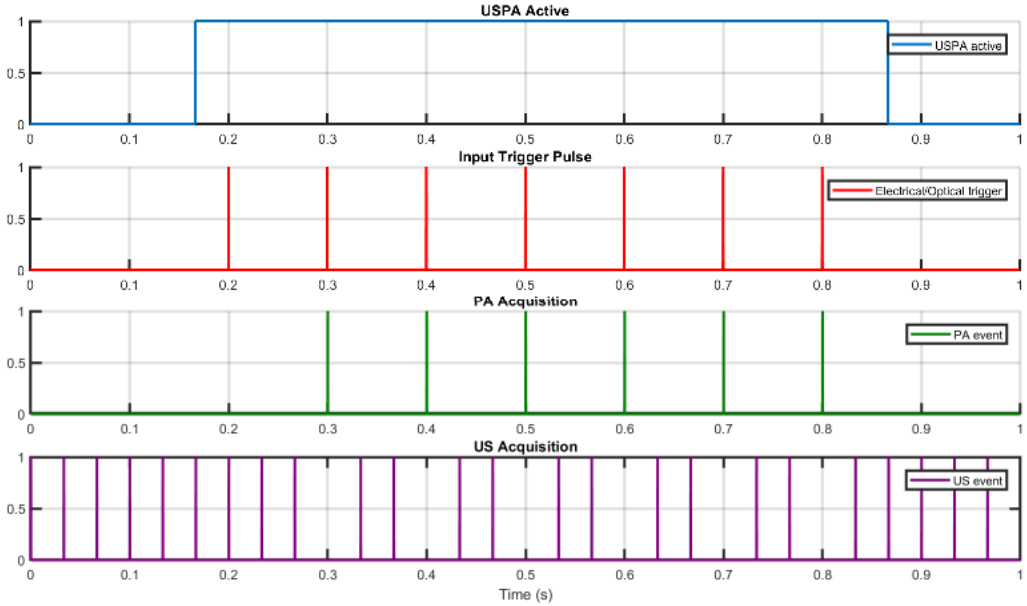

Figure 3: Timing diagram of the USPA system's communication. Example with 10 Hz laser, US continuous mode.

3. EXPERIMENTAL SETUP

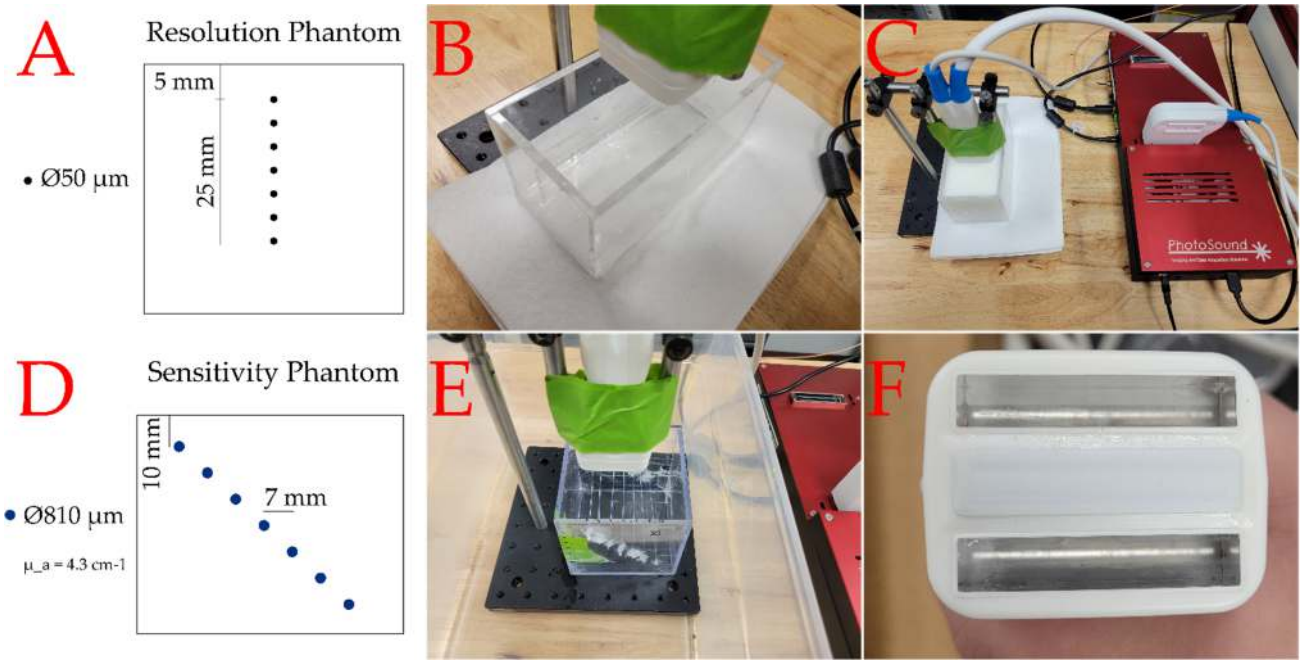

Figure 4: Phantom experiment setup. Spatial resolution phantom diagram (A), spatial resolution phantom setup (B), full imaging setup, except for the laser (C), depth sensitivity phantom diagram (D), depth sensitivity phantom setup (E), probe face with detector array and fiberoptic outputs (F).

To get some first results using the USPA system, two phantoms were prepared and imaged: a spatial resolution phantom (Figure 4:A,B) and a depth sensitivity phantom (Figure 4:D,E). The laser excitation source (Phocus Mobile HE, Opotek, Carlsbad, CA, USA) had a repetition rate of 10 Hz and, when coupled with the probe's fiberoptics, had a fluence of 2.60 ± 0.07 mJ/cm^2 at 800 nm, the wavelength used for the phantom scans. The US probe (OA-16-1S, Seno Medical, San Antonio, TX, USA) was a 128-channel linear 38.4 mm transducer with an integrated fiberoptic bundle split into two outputs (Figure 4:F). It had a PA central frequency response of 9.4 ± 0.9 MHz with bandwidth >80% and a US frequency range of 5-14 MHz, the focal depth of the probe was 20 mm. The MoleculUS system was attached to the PC via USB3 for both the US and PA modes and triggered by the laser's electrical trigger output.

The spatial resolution phantom consisted of seven Ø50 µm black nylon monofilaments spaced vertically by 5 mm, with a 5 mm initial depth from the probe face, in an acrylic box. The phantom was filled with a scattering medium of 13 parts 2% milk to 18 parts deionized water to mimic breast tissue [18]. The probe was fixed above the phantom with detector array perpendicular to the length of the monofilaments (Figure 4:C). The depth sensitivity phantom had seven Ø810 µm polytetrafluoroethylene microcuvettes filled with $CuSO_4 \bullet 5H_2O$ (143.2 g/l) μ_a = 4.3 cm^{-1} at 800 nm, the mean μ_a for blood at 800 nm [19] (Figure 4:D). The microcuvettes were vertically spaced 10 mm and horizontally spaced 7 mm from one another and had their cross-sections scanned three times, with a horizontal translation of the probe each scan to acquire data from all microcuvettes. All scans acquired 100 frames of US and PA data, synchronized, with US T/R frequency set to 12 MHz.

The spatial resolution phantom PA signals acquired were averaged and reconstructed with voxel size 20 µm. The monofilament at depth closest to 20 mm had its horizontal and vertical line profiles fitted with a gaussian to estimate the spatial resolution, using the calculated full width at half max (FWHM) as the estimate. The depth sensitivity phantom also had its PA signals averaged, but reconstructed with voxel size 100 µm. The microcuvettes and local background were segmented and the contrast-to-noise ratio (CNR) was calculated according to equation (1) [20].

$$CNR = \frac{I_{tgt} - I_{Bkg}}{\sqrt{\sigma_{tgt}^2 + \sigma_{Bkg}^2}}$$

(1)

Where I_{tgt} is the segmented microcuvette mean target inclusion, I_{Bkg} is the mean background, σ_{tgt}^2 is the variance of the target inclusion, and σ_{Bkg}^2 is the variance of the background.

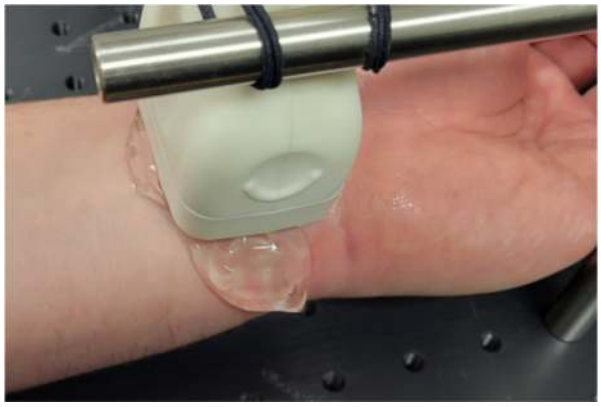

Figure 5: Imaging a human wrist *in vivo* with the USPA system.

Finally, using the same experimental setup, a human wrist was imaged in vivo while it was rotating. The PA reconstructions are not averaged and have voxel size of 100 µm.

4. RESULTS

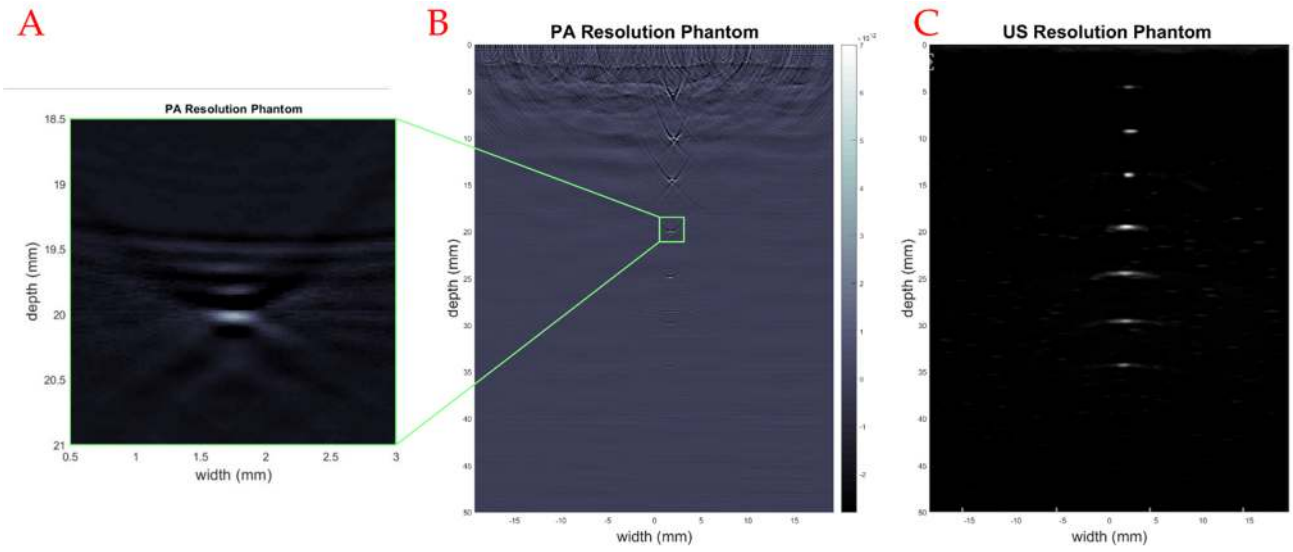

Figure 6: PA spatial resolution phantom image with "bone" colormap, US with greyscale colormap. A zoomed portion of the PA reconstruction with modified dynamic range was analyzed for spatial resolution (A). The full PA phantom depth (B). The full US phantom depth (C).

The PA image reconstruction of the spatial resolution phantom has all seven monofilaments visible up to a depth of ≈ 35 mm (Figure 6:B), matching the US image reconstruction of the same phantom (Figure 6:C). A zoomed in area of the

monofilament closest to the probe's focal depth, 20 mm, was analyzed for its PA spatial resolution (Figure 6:A). The PA spatial resolution was calculated as 89 µm in depth and 309 µm in width.

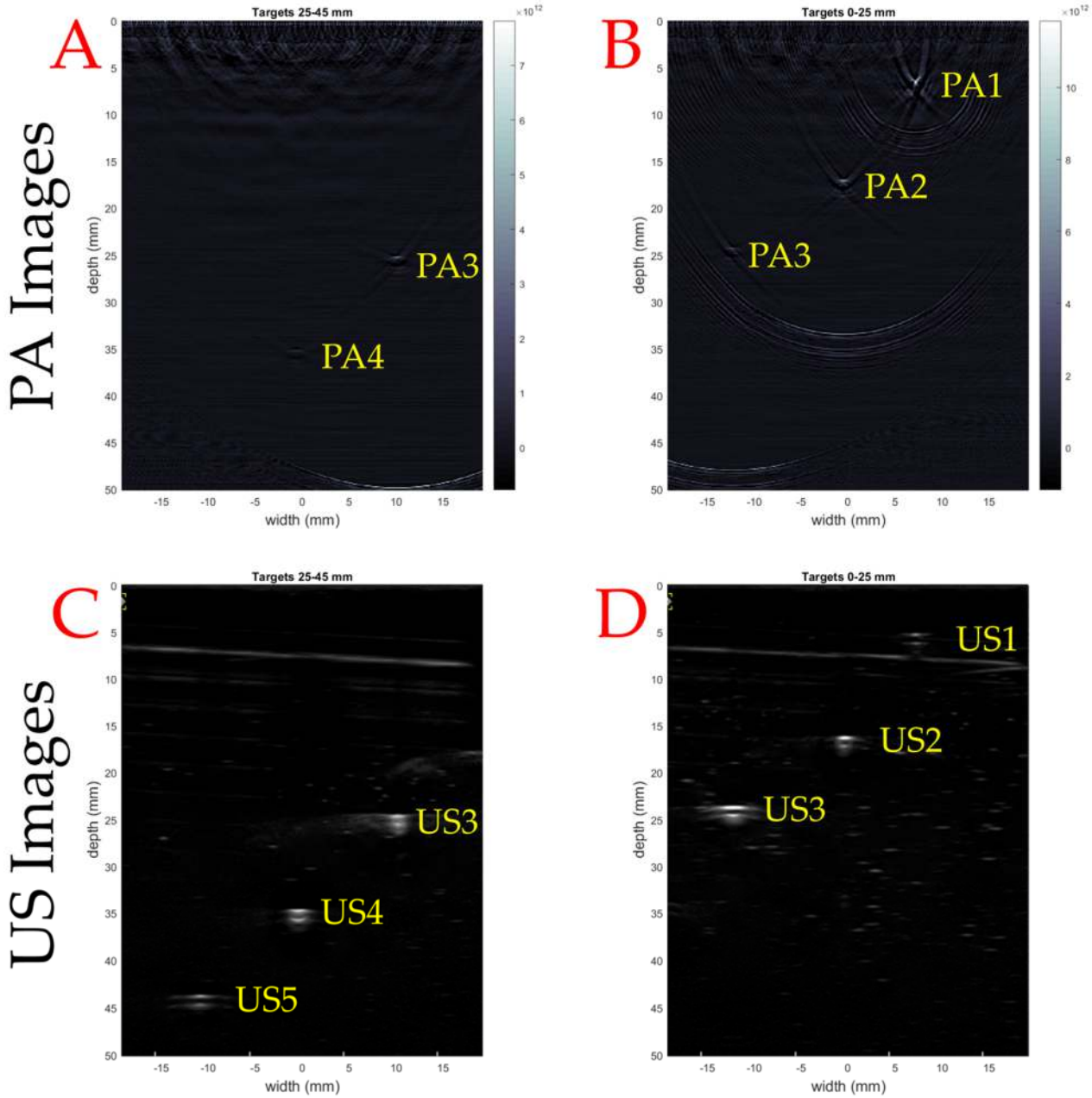

Figure 7: Depth sensitivity phantom. The PA reconstruction images of the depth sensitivity phantom at two height windows (A, B). The US reconstruction images of the depth sensitivity phantom at two height windows (C, D). The detected microcuvettes filled with samples are labeled as PA/US (1, 2, 3, 4, 5).

The depth sensitivity phantom's results show that the deepest visible sample in the PA image was the microcuvette at 35 mm (Figure 7:A:PA4) while the US image could detect deeper samples (Figure 7:A:US5). The CNR of each sample visualized in PA is in Table 1.

Table 1: CNR values of samples detected in PA images.

Sample depth (mm)	PA CNR
7	3.08
17	2.59
24	1.84
36	1.09

An example two frames, of the 100 acquired with motion, of the in vivo human wrist imaging are shown in Video 1. Surface vessels are visible near the skin (depth 0-5 mm) and the radial artery can be seen pulsing at the beginning of the video near the width 15 mm, depth 10 mm coordinates.

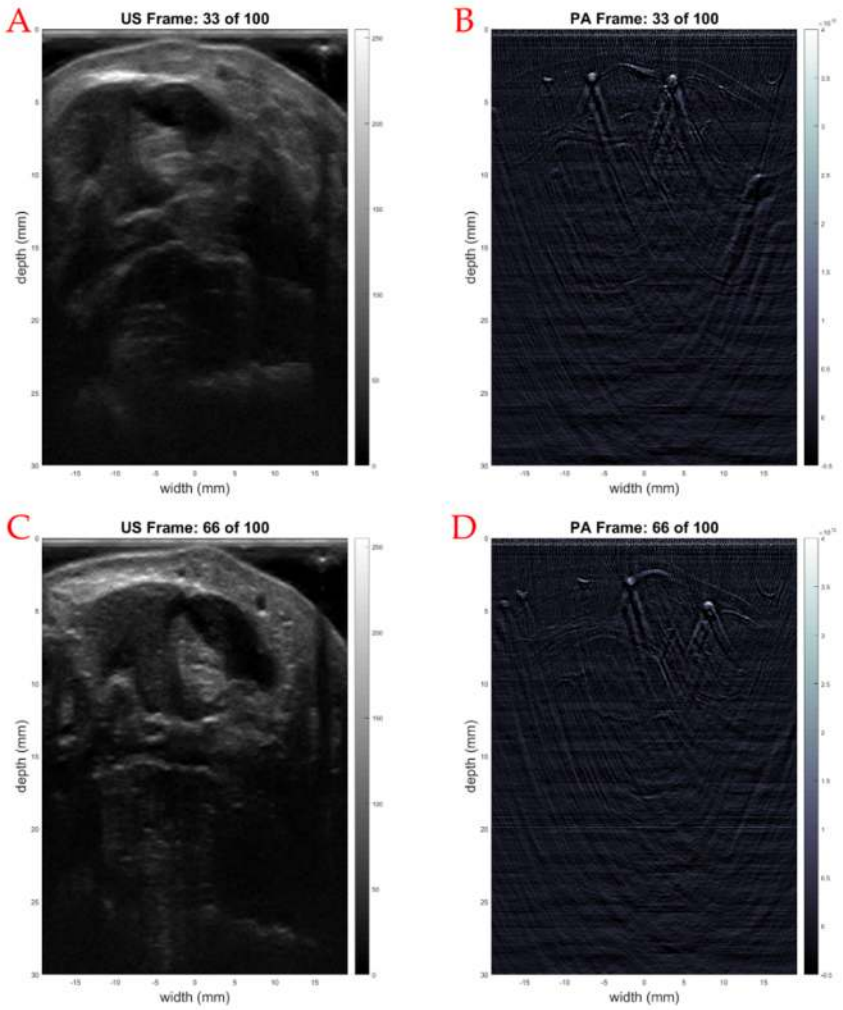

Video 1: Wrist PA and US images. Frame #33/100 US (A) and PA (B) reconstructed images. Frame #66/100 US (C) and PA (D) reconstructed images. http://dx.doi.org/10.1117/12.2610099

5. CONCLUSION

We detailed the hardware of a USPA imaging system, the MoleculUS, and its features. A phantom demonstration of the MoleculUS was performed and we measured detection estimates of the described experimental setup. The PA spatial resolution results show that, at the probe's focal depth, the estimated depth resolution of the monofilament was 89 µm compared to an actual diameter of 50 µm. The background noise of the full PA depth image (Figure 6:B) was substantial and determined to be caused by electrical interference between the US/PA modes and will be accounted for in the future. All seven high absorbing monofilaments are visible in the full depth PA image.

The tissue-mimicking depth sensitivity phantom's interpolated PA results estimated the imaging depth of the setup to be reasonable up to ≈ 23 mm for a CNR >2. The US results show the imaging depth to be further than the PA mode, up to at least 65 mm (Figure 8).

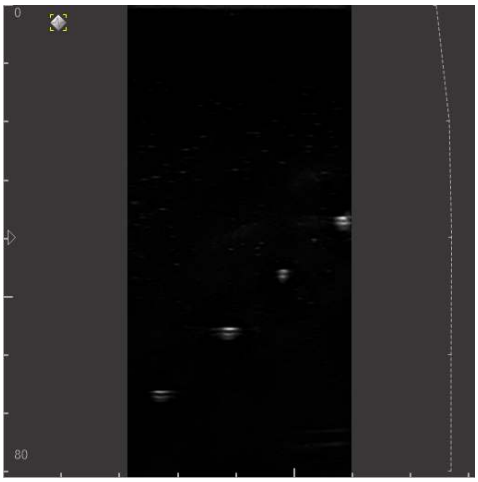

Figure 8: US image of depth sensitivity phantom, phantom height window 35 – 65 mm, full depth scale from 0 – 80 mm.

The *in vivo* human wrist imaging video had superficial vessels visible as well as deeper tissue, such as the radial artery, detected in both US and PA modes and is a promising first step in future clinical studies. All of the images were acquired with a relatively low fluence of 2.6 mJ/cm^2, well below the American National Standard (ANSI Z136.3) limitations for 800 nm (20 mJ/cm^2), which suggests future studies with higher energies could have improved CNR results. Future experiments with different probes and phantoms will be performed to further characterize the MoleculUS as well as investigating more potential *in vivo* application of the system.

ACKNOWLEDGEMENT

This work is supported in part by the National Institutes of Health grant 1R37CA240806-01A1 (National Cancer Institute). Thanks to TELEMED for the joint development of the USPA MoleculUS system and to Seno Medical for lending their probe.

REFERENCES

[1] L. Abou-Elkacem, S. V. Bachawal, and J. K. Willmann, "Ultrasound molecular imaging: Moving toward clinical translation," *European Journal of Radiology,* vol. 84, no. 9, pp. 1685-1693, 2015-09-01 2015, doi: 10.1016/j.ejrad.2015.03.016.

[2] C. M. Moran and A. J. W. Thomson, "Preclinical Ultrasound Imaging—A Review of Techniques and Imaging Applications," (in English), *Frontiers in Physics,* Review vol. 8, 2020-May-05 2020, doi: 10.3389/fphy.2020.00124.

[3] S. C. Hester, M. Kuriakose, C. D. Nguyen, and S. Mallidi, "Role of Ultrasound and Photoacoustic Imaging in Photodynamic Therapy for Cancer," *Photochemistry and Photobiology,* vol. 96, no. 2, pp. 260-279, 2020, doi: 10.1111/php.13217.

[4] S. Y. Emelianov, P.-C. Li, and M. O'Donnell, "Photoacoustics for molecular imaging and therapy," (in eng), *Physics today,* vol. 62, no. 8, pp. 34-39, 2009, doi: 10.1063/1.3141939.

[5] A. B. E. Attia *et al.*, "A review of clinical photoacoustic imaging: Current and future trends," *Photoacoustics,* vol. 16, p. 100144, 2019-12-01 2019, doi: 10.1016/j.pacs.2019.100144.
[6] C. Bench, A. Hauptmann, and B. Cox, "Toward accurate quantitative photoacoustic imaging: learning vascular blood oxygen saturation in three dimensions," *Journal of Biomedical Optics,* vol. 25, no. 08, 2020-08-24 2020, doi: 10.1117/1.jbo.25.8.085003.
[7] M. Li, Y. Tang, and J. Yao, "Photoacoustic tomography of blood oxygenation: A mini review," *Photoacoustics,* vol. 10, pp. 65-73, 2018/06/01/ 2018, doi: https://doi.org/10.1016/j.pacs.2018.05.001.
[8] T. Zhao, A. E. Desjardins, S. Ourselin, T. Vercauteren, and W. Xia, "Minimally invasive photoacoustic imaging: Current status and future perspectives," *Photoacoustics,* vol. 16, p. 100146, 2019/12/01/ 2019, doi: https://doi.org/10.1016/j.pacs.2019.100146.
[9] I. Steinberg, D. M. Huland, O. Vermesh, H. E. Frostig, W. S. Tummers, and S. S. Gambhir, "Photoacoustic clinical imaging," *Photoacoustics,* vol. 14, pp. 77-98, 2019, doi: 10.1016/j.pacs.2019.05.001.
[10] C. Bench and B. Cox, "Quantitative photoacoustic estimates of intervascular blood oxygenation differences using linear unmixing," *Journal of Physics: Conference Series,* vol. 1761, p. 012001, 01/01 2021, doi: 10.1088/1742-6596/1761/1/012001.
[11] S. Tzoumas and V. Ntziachristos, "Spectral unmixing techniques for optoacoustic imaging of tissue pathophysiology," *Philosophical Transactions of the Royal Society A: Mathematical, Physical and Engineering Sciences,* vol. 375, no. 2107, p. 20170262, 2017-11-28 2017, doi: 10.1098/rsta.2017.0262.
[12] Y. Yan *et al.*, "Endocavity ultrasound and photoacoustic system for fetal and maternal imaging: design, implementation, and ex-vivo validation," *Journal of Medical Imaging,* vol. 8, no. 6, p. 066001, 2021.
[13] S. Wang, Y. Zhao, and Y. Xu, "Recent advances in applications of multimodal ultrasound-guided photoacoustic imaging technology," *Visual Computing for Industry, Biomedicine, and Art,* vol. 3, no. 1, 2020-12-01 2020, doi: 10.1186/s42492-020-00061-x.
[14] J. Kim, E.-Y. Park, B. Park, W. Choi, K. J. Lee, and C. Kim, "Towards clinical photoacoustic and ultrasound imaging: Probe improvement and real-time graphical user interface," *Experimental Biology and Medicine,* vol. 245, no. 4, pp. 321-329, 2020, doi: 10.1177/1535370219889968.
[15] C. Kim, T. N. Erpelding, L. Jankovic, and L. V. Wang, "Performance benchmarks of an array-based hand-held photoacoustic probe adapted from a clinical ultrasound system for non-invasive sentinel lymph node imaging," *Philosophical Transactions of the Royal Society A: Mathematical, Physical and Engineering Sciences,* vol. 369, no. 1955, pp. 4644-4650, 2011-11-28 2011, doi: 10.1098/rsta.2010.0353.
[16] W. Thompson, H. P. Brecht, S. Ermilov, and V. Ivanov, *Massive parallel ultrasound and photoacoustic PC-based system* (SPIE BiOS). SPIE, 2020.
[17] V. Ivanov, H. Brecht, and S. Ermilov, *Real-time photoacoustic data acquisition with a thousand parallel channels at hundreds frames per second* (SPIE BiOS). SPIE, 2019.
[18] S. Ermilov *et al.*, *Real-time optoacoustic imaging of breast cancer using an interleaved two laser imaging system coregistered with ultrasound* (SPIE BiOS). SPIE, 2010.
[19] N. Bosschaart, G. J. Edelman, M. C. G. Aalders, T. G. Van Leeuwen, and D. J. Faber, "A literature review and novel theoretical approach on the optical properties of whole blood," *Lasers in Medical Science,* vol. 29, no. 2, pp. 453-479, 2014-03-01 2014, doi: 10.1007/s10103-013-1446-7.
[20] M. S. Patterson and F. S. Foster, "The improvement and quantitative assessment of B-mode images produced by an annular array/cone hybrid," (in eng), *Ultrason Imaging,* vol. 5, no. 3, pp. 195-213, Jul 1983, doi: 10.1177/016173468300500301.